Mathematical Model of the Thermal Processing of Steel Ingots: Part II. Stress Model

B. G. THOMAS, I. V. SAMARASEKERA, and J. K. BRIMACOMBE

A mathematical model has been developed to predict the internal stresses generated in a steel ingot during thermal processing. The thermal history of the ingot has been predicted by a finite-element, heat-flow model, the subject of the first part of this two-part paper, which serves as input to the stress model. The stress model has been formulated for a two-dimensional transverse plane at mid-height of the ingot and is a transient, elasto-viscoplastic, finite-element analysis of the thermal stress field. Salient features of the model include the incorporation of time-temperature and temperature-dependent mechanical properties, and volume changes associated with nonequilibrium phase transformation. Model predictions demonstrate that the development of internal stresses in the ingot during thermal processing can be directly linked to the progress of the phase transformation front. Moreover, the low strain levels calculated indicate that metallurgical embrittlement must be very important to the formation of cracks in addition to the development of high tensile stresses.

I. INTRODUCTION

THE importance of predicting the thermal stresses in a steel ingot during processing, in an effort to understand the mechanisms for the formation of defects such as panel cracks, cannot be over-emphasized. Although a number of studies have been undertaken to elucidate the role of factors such as thermal history, stress generation, and ductility loss on panel crack formation, these have been qualitative and no numerical stress model has yet been utilized.

Until recently, the modeling of thermal stresses in casting processes has involved crude "strength of materials" approaches and therefore has had only limited application. Only with the advent of more sophisticated computer modeling techniques is the capability to simulate stress generation more accurately being developed. Advanced numerical stress models, including the effects of creep, have now been successfully applied to continuous casting,[1-6] but models previously developed for ingot casting[7,8,9] have ignored creep and only two have considered the effects of phase transformation.[7,9]

This paper, which is the second of a two-part study,[10] describes the development, verification, and application of a mathematical model which calculates the thermal stresses generated in an ingot during solidification in the mold, air cooling, and subsequent reheating in the soaking pit. The model relies on the heat-flow analysis described in the first part for predictions of the thermal field and is based on the premise that uncoupling of the heat flow and stress models is realistic in view of the negligible effect heat generated by in-elastic deformation has on the slowly changing thermal field.

Because the impetus for developing the stress model was to understand the mechanisms leading to panel crack formation in aluminum-killed steel ingots, property data and assumptions made in the formulation of the model reflect this end use. The variables chosen to describe quantitatively the development of thermal stresses during steel ingot processing are linked to well known fracture criteria and lay the groundwork for later papers in which the mechanisms governing the formation of these defects are elucidated.

II. MODEL FORMULATION

The model has been formulated for a two-dimensional, one-quarter, transverse section through the ingot at mid height, for reasons elucidated in Part I.[10] A state of plane stress was assumed and only small strains were considered. Thus, the stress distribution within the two-dimensional solid region is governed by:

$$\frac{\partial \sigma_x}{\partial x} + \frac{\partial \tau_{xy}}{\partial y} = 0 \qquad [1]$$

$$\frac{\partial \sigma_y}{\partial y} + \frac{\partial \tau_{xy}}{\partial x} = 0 \qquad [2]$$

where σ_x, σ_y are the internal stresses in the ingot normal to the x and y planes, respectively. Stresses in the mold were not computed, for economy.

The standard "displacement formulation" was used to relate stress increments, $\{\Delta\sigma\}$, to displacement increments, $\{u, v\}^{-1}$, through the "kinematic relations":

$$\{\Delta\varepsilon\} = \begin{bmatrix} \partial/\partial x & 0 \\ 0 & \partial/\partial y \\ \partial/\partial y & \partial/\partial x \end{bmatrix} \begin{Bmatrix} u \\ v \end{Bmatrix} \qquad [3]$$

and the constitutive equations for an elastic, plane-stress, isotropic condition:

$$\{\Delta\sigma\} = [E]\{\Delta\varepsilon_e\} \qquad [4]$$

where

$$[E] = \frac{E}{(1 - \nu^2)} \begin{bmatrix} 1 & \nu & 0 \\ \nu & 1 & 0 \\ 0 & 0 & \dfrac{1-\nu}{2} \end{bmatrix} \qquad [5]$$

B. G. THOMAS, formerly a Graduate Student at the University of British Columbia, is Assistant Professor in the Department of Mechanical and Industrial Engineering, University of Illinois, 1206 West Green Street, Urbana, IL 61801. I. V. SAMARASEKERA, Associate Professor, and J. K. BRIMACOMBE, Stelco/NSERC Professor and Director, are with The Centre for Metallurgical Process Engineering at the University of British Columbia, Vancouver, BC, Canada, V6T 1W5.
Manuscript submitted February 3, 1986.

METALLURGICAL TRANSACTIONS B VOLUME 18B, MARCH 1987—131

and E is temperature dependent and ν is temperature independent. The incremental total strain vector, $\{\Delta\varepsilon\}$, was divided into three parts in order to relate it to the elastic strain increments, $\{\Delta\varepsilon_e\}$:

$$\{\Delta\varepsilon\} = \{\Delta\varepsilon_e\} + \{\Delta\varepsilon_T\} + \{\Delta\varepsilon_p\} \quad [6]$$

$\{\Delta\varepsilon_T\}$ and $\{\Delta\varepsilon_p\}$ contain the incremental thermal strain components and plastic creep strain components, respectively.

A. Boundary Conditions

These equations are subject to the boundary conditions illustrated schematically in Figure 1 for the 760×1520 mm steel ingot. To impose two-fold symmetry, one degree of freedom was removed along each centerline by imposing the specified displacement boundary conditions:

$$t \geq 0, \quad y = 0, \quad 0 \leq x \leq 0.380, \quad u = 0$$
$$[7]$$

$$t \geq 0, \quad x = 0, \quad 0 \leq y \leq 0.760, \quad v = 0$$
$$[8]$$

The conditions in Eqs. [7] and [8] remove both degrees of freedom from the center of the ingot $(0, 0)$ to prevent rigid body motion.

Over the remaining exterior surface of the ingot, no applied surface tractions were imposed. This boundary condition assumes that no sticking occurs in the mold. This is reasonable, since any stresses arising due to sticking would occur early during solidification and could only lead to "hot tearing", a cracking problem involving high temperature embrittlement that is different from panel cracking. Previous work indicates that panel cracks form through a different mechanism involving intermediate temperature ductility losses and occur much later during ingot processing.[12]
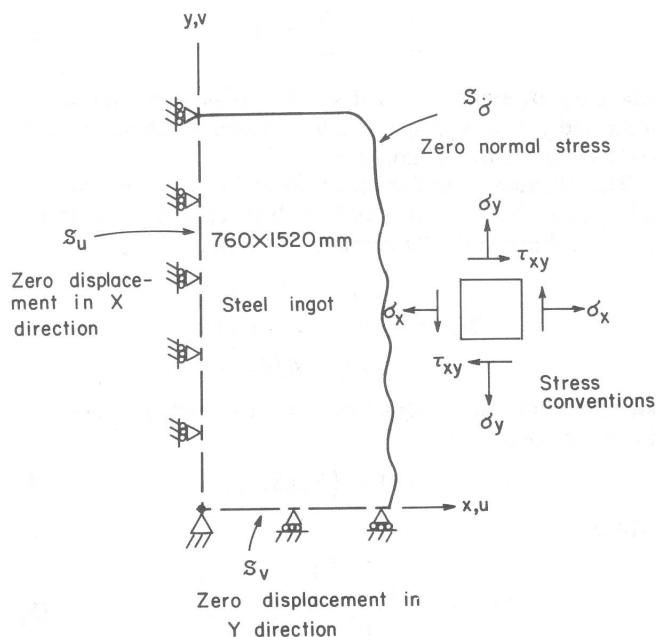

Fig. 1—Stress model boundary conditions.

B. Thermal Strain

The volume changes that accompany changing temperature gradients are traditionally accounted for in thermal stress models through a constant thermal expansion coefficient.[1,3,8,11,13] This results in an incremental thermal strain vector:

$$\{\Delta\varepsilon_T\} = \begin{Bmatrix} \alpha(T_{t+\Delta t} - T_t) \\ \alpha(T_{t+\Delta t} - T_t) \\ 0 \end{Bmatrix} = \begin{Bmatrix} \alpha\,\Delta T \\ \alpha\,\Delta T \\ 0 \end{Bmatrix} \quad [9]$$

where $T_{t+\Delta t}$ and T_t define the change in temperature over a time interval for which the resulting stresses are to be calculated. However, the temperature dependence of α for steel cannot be ignored in this analysis owing to the wide range of temperatures encountered in the thermal processing of ingots. In addition, the volume changes caused by phase transformation are significant and must be included. A method, which is capable of handling any type of volume change, was adopted in this model to account for the expansion and contraction associated with phase transformations. Thermal linear expansion was used as a state function in an analogous manner to the use of enthalpy, in heat transfer modeling, instead of specific heat:

$$TLE(T) = \int_{T_0}^{T} \alpha(T)\,dT \quad [10]$$

where T_0 is an arbitrary base temperature, assumed equal to 0 °C. The model then calculates thermal strain increments from the temperatures generated by the heat flow model:

$$\{\Delta\varepsilon_T\} = \begin{Bmatrix} TLE(T_{t+\Delta t}) - TLE(T_t) \\ TLE(T_{t+\Delta t}) - TLE(T_t) \\ 0 \end{Bmatrix} \quad [11]$$

The model then requires the thermal linear expansion of the desired steel to be input as a function of temperature, including the strains resulting from phase transformations.

C. Plastic-Creep Strain

In addition to the thermal strain, the stress model must also account for the time- and temperature-dependent plastic flow behavior of steel, including strain due to creep. This has a profound influence on stress generation at the elevated temperatures and low strain rates encountered during ingot casting. Unfortunately, it has been neglected in previous ingot stress models.[7–9,11]

In previous work, time-independent plastic flow and creep often have been treated separately. However, the strain generated by creep is physically indistinguishable from that resulting from time-independent plastic flow. Both are incompressible and irrecoverable. Particularly at higher temperatures, where experimental observations are difficult and only the combined effect is measurable, there is little justification for dividing plastic strain into two types. The distinction is, at best, only an analytical convenience.[14]

Part of the confusion arises because the time-dependent, plastic flow behavior of metals at elevated temperatures has been studied experimentally using several different uniaxial testing methods. The first is standard tensile testing where a fixed strain rate is applied to a specimen and the resulting

stress is recorded as a function of plastic strain. This leads to mathematical descriptions of the behavior in terms of "strain hardening":

$$\sigma = f(\dot{\varepsilon}_{\mathbf{p}}, T, \varepsilon_{\mathbf{p}}) \qquad [12]$$

The second method is the standard creep test, where a fixed stress is applied and the resulting strain is recorded as a function of time. This gives rise to "time-hardening" descriptions involving creep or creep rate functions. For example:

$$\varepsilon_{\mathbf{p}} = f(\sigma, T, t) \qquad [13]$$

A third method is stress relaxation which examines time-dependent plastic flow under constant strain. This results in "time-softening" expressions for stress:

$$\sigma = f(\varepsilon_{\mathbf{p}}, T, t) \qquad [14]$$

These seemingly different phenomena are all simply different manifestations of a single, complex relationship between σ, $\varepsilon_{\mathbf{p}}$, T, and t or $\dot{\varepsilon}_{\mathbf{p}}$. The present model incorporates a more general description of time-dependent, plastic flow which lumps both creep and plastic strain rates together as a single "plastic creep" strain rate:

$$\dot{\varepsilon}_{\mathbf{p}} = f(\sigma, T, \text{structure}) \qquad [15]$$

The structure parameter, which characterizes the resistance to plastic flow offered by the internal microstructural state of the material, could be represented by a number of variables such as accumulated plastic strain, time, or dislocation density.[14] The plastic-creep strain rate, $\dot{\varepsilon}_{\mathbf{p}}$, is a scalar function based on uniaxial test data for steel which was input to the model over appropriate stress, strain rate, and temperature ranges. The components of the incremental "plastic-creep strain" vector, $\{\Delta \varepsilon_{\mathbf{p}}\}$, required by the stress model, were calculated from $\dot{\varepsilon}_{\mathbf{p}}$ using the Prandtl-Reuss relations for associated plasticity in plane stress, and the Von Mises effective stress parameter.[14,15,16]

This formulation can be classified as an elasto-viscoplastic thermal stress model.[14] It provides both a simple and physically reasonable mathematical treatment of plasticity which could be employed to provide computationally efficient solutions to both pure elasto-creep problems and time-independent plasticity problems.

III. SOLUTION TECHNIQUE

The solution technique developed for the present model was based on a method developed by Zienkiewicz and Cormeau[14] combined with approaches taken in other studies.[13,17,18]

Using standard finite-element techniques to reformulate and solve the elasto-viscoplastic thermal stress problem described mathematically by Eqs. [1] through [8], [11], and [15] results in a set of simultaneous equations, to be solved at each time step for the unknown nodal displacements, $\{d\}$, which contain the x and y displacements, u and v, for each node in the mesh:

$$[K_{\sigma}]\{d\} = \{\mathbf{F}_{\varepsilon\mathbf{T}}\} + \{\mathbf{F}_{\varepsilon\mathbf{p}}\} \qquad [16]$$

The global stiffness matrix, $[K_{\sigma}]$, global thermal force vector, $\{\mathbf{F}_{\varepsilon\mathbf{T}}\}$, and global plastic strain force vector, $\{\mathbf{F}_{\varepsilon\mathbf{p}}\}$, are found by summing the contributions from individual elements:

$$[K_{\sigma}] = \sum_{i=1}^{NE} [K_{\sigma}]_i^e = \sum_{i=1}^{NE} \int_A \int [B]_i^{eT}[E]_i[B]_i^e \, dA \qquad [17]$$

$$\{\mathbf{F}_{\varepsilon\mathbf{T}}\} = \sum_{i=1}^{NE} \{\mathbf{F}_{\varepsilon\mathbf{T}}\}_i^e = \sum_{i=1}^{NE} \int_A \int [B]_i^{eT}[E]_i\{\Delta\varepsilon_0\} \, dA \qquad [18]$$

$$\{\mathbf{F}_{\varepsilon\mathbf{p}}\} = \sum_{i=1}^{NE} \{\mathbf{F}_{\varepsilon\mathbf{p}}\}_i^e = \sum_{i=1}^{NE} \int_A \int [B]_i^{eT}[E]_i\{\Delta\varepsilon_p\} \, dA \qquad [19]$$

$[B]^e$ is the 3×6 matrix containing the displacement gradients for the constant strain triangle.[16,19]

The spatial continuum was divided into three-node, constant-strain, triangular finite elements which matched the nodal scheme employed in the heat-transfer model, permitting direct input of temperature. These simple elements were chosen over higher order elements because nonlinearities, such as the discontinuous stress field across the solid-liquid boundary, would be better approximated by a large number of elements than by fewer elements each having more degrees of freedom. In addition, the same element mesh data could be employed after discarding the mold elements and renumbering the ingot nodes to reduce the bandwidth. Figure 2 illustrates the 330 node, 575-element mesh constructed to model the 760 × 1520 mm (30 × 60 in.), 23,000-kg steel ingot chosen to represent a typical off-corner, panel-cracked ingot size.
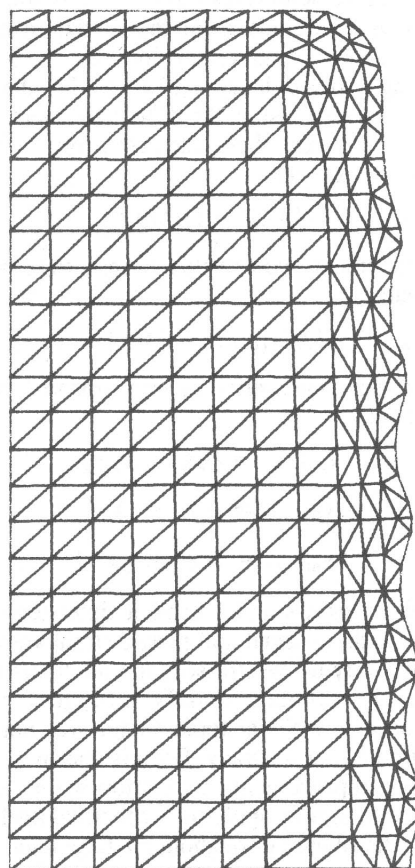

Fig. 2 — Finite-element mesh used for stress analysis of a 760 × 1520 mm, 23,000 kg corrugated ingot.

Variables that define the state of the ingot were initialized and tracked for each node in the mesh as time proceeded. These included the temperature, total strain components, total plastic-creep strain components, total stress components, the fraction austenite transformed, and the direction of heating/cooling. Within each element, a constant elastic modulus was calculated at each time step by using nodal temperature input from the heat-transfer model:

$$E^e = \frac{1}{6}[E(T_{1,t\Delta t}) + E(T_{2,t+\Delta t}) + E(T_{3,t+\Delta t})$$
$$+ E(T_{1,t}) + E(T_{2,t}) + E(T_{3,t})] \qquad [20]$$

Poisson's ratio was assumed to remain constant with a value of 0.3. With increasing temperature or decreasing strain rate, ν has been observed experimentally to increase, reaching a maximum of almost 0.5.[20] However, this merely reflects the increase in incompressible plastic flow due to creep which the model takes into account separately.

Plastic strain rate values, $\dot{\varepsilon}_p$, were calculated for each node at the beginning of each time step based on the previously known stress state and average temperature over the time interval. In evaluating $\dot{\varepsilon}_p$, precautions were taken in the model numerically to ensure that the sense of $\dot{\varepsilon}_p$ was in the same direction as the stress. Plastic-creep strains for the time interval were then evaluated from:

$$\Delta\varepsilon_p = \Delta t\dot{\varepsilon}_p \qquad [21]$$

Incremental thermal loads for the time step, $\{\Delta\varepsilon_T\}$, were calculated for each node using Eq. [11]. Fixed degrees of freedom were then achieved simply by removing the appropriate rows and columns from the global matrices. The banded, symmetric, matrix equation, Eq. [16], was then assembled and solved in core memory for the unknown nodal displacements using the Cholesky method.[21] Total strain increments were then calculated from the displacements with the expression:

$$\{\Delta\varepsilon\}^e = [B]\{d\}^e \qquad [22]$$

and stress increments were evaluated from the strains within each element:

$$\{\Delta\sigma\}^e = [E](\{\Delta\varepsilon\}^e - \{\Delta\varepsilon_p\} - \{\Delta\varepsilon_T\}) \qquad [23]$$

Finally, the total state variables were updated prior to the next time step:

$$\{\sigma\}_{t+\Delta t} = \{\sigma\}_t + \{\Delta\sigma\} \qquad [24]$$

$$\{\varepsilon\}_{t+\Delta t} = \{\varepsilon\}_t + \{\Delta\varepsilon\} \qquad [25]$$

$$\{\varepsilon_p\}_{t+\Delta t} = \{\varepsilon_p\}_t + \{\Delta\varepsilon_p\} \qquad [26]$$

The model uses a simple, explicit time-stepping procedure. Because the thermal and plastic strain vectors do not contribute directly to the stresses, and nonlinearity is introduced into the problem mainly through these terms, minimization of a residual force vector was not very productive in improving accuracy. For this reason, it was found that accuracy improvement by iteration within a time step was achieved by simply applying the thermal load in smaller increments, distributed throughout the time interval. This is equivalent to using smaller time steps and it allows all of the nonlinearities in the problem to approach more closely the linear approximation inherent to the calculation procedure.

Use of the same global stiffness matrix, $[K_\sigma]$, for several time steps allowed a substantial reduction in computing costs and is similar to the modified Newton-Raphson method used in the initial stress approach for elasto-plastic problems.[16,18]

Because the time-integration procedure is explicit in nature, it is prone to instability if the nonlinearities are too large. This was partially overcome through the introduction of variable time steps which also were used in the heat-transfer model. Smaller time steps were employed both initially and at times when the temperature and stresses were changing rapidly. At other times, the linear approximations of the model were valid over longer time intervals.

Unfortunately, the optimum time step size is very difficult to estimate and is the subject of ongoing research. To overcome stability problems that were occasionally encountered, a truncating function subroutine was built into the program. This limited the maximum size of a plastic creep strain increment in any time step to 5 pct of the total effective plastic strain accumulated up to that time. The value of 5 pct falls in the 1 to 15 pct range suggested by Zienkiewicz and Cormeau[14] and was found to prevent instability in all cases. Naturally, severely-truncated model runs would underpredict creep strain and therefore overpredict stress. By recording the extent of truncation, these inaccuracies could be anticipated and subsequently avoided.

The model, including pre- and post-processing routines, was coded into FORTRAN IV programs and run on the UBC Amdahl 470/V8 computer.

IV. THERMOMECHANICAL PROPERTY DATA

The accuracy of stress model predictions has been limited in the past by the lack of a general constitutive equation and appropriate experimental data with which to quantify the visco-plastic behavior described in Eq. [15].

A. Plastic-Creep Strain Rate Function

The search for a state function to characterize the structure parameter in Eq. [15] is a difficult task which has received recent attention.[22,23,24] Experimental data from constant stress and constant strain (stress relaxation) tests are usually expressed as functions of time, which is obviously a very poor state variable with which to characterize structure during the processing of a steel ingot. While the strain hardening relationships developed from constant strain rate test data are better, they still model high-temperature softening behavior very poorly. In view of these deficiencies, the inclusion of a structure parameter was judged to be premature. Thus, as a first approximation, data were used to fit an equation of the form:

$$\dot{\varepsilon}_p = f(\sigma, T) \qquad [27]$$

This is equivalent to assuming the constant structure condition of secondary creep in the creep test and zero strain hardening in the tensile test. It is a fairly reasonable approximation for the behavior of steel at elevated temperatures and has been incorporated in previous models.[2,6]

To model the medium-carbon steels affected by mid-face panel cracking, a relationship developed by Wray was adopted:[20]

$$\dot{\varepsilon}_p = 907 \times 10^{10}[\sinh(0.0356\overline{\sigma})]^{6.90} \exp\left(\frac{-41938}{T + 273}\right)$$ [28]

This equation was based on flow stress data from tensile tests conducted on 0.46 pct C steel at intermediate strain-rate in the austenite phase at a plastic strain of 0.2 pct. It predicts mechanical behavior similar to that of the data reported by other researchers.[25,26]

Not surprisingly, the influence of temperature on the plastic deformation of steel was found to be approximately the same regardless of the nature of the experimental test (constant stress or constant strain rate) — an Arrhenius relationship with an activation energy equal to that of iron self-diffusion in the range 200 to 340 kJ/g mole.[20,27–29] Pines and Sirenko[30] report that the temperature dependence of creep rate in steel is determined solely by the self-diffusion coefficient of iron. However, the self-diffusion coefficient of α iron is three hundred[31] to one thousand[32] times larger than that of γ at the same temperature. In addition, several other studies have either noted or implied accelerated creep in the softer ferrite phase of low-carbon steels.[26,32–35] Thus,

Fig. 3—Plastic creep strain rate function used for low-carbon steel.

to model low-carbon, (0.15 pct C) steel, a modified version of a relationship developed by Wray[20] was adopted:

$$\dot{\varepsilon}_p = A_0[\sinh(0.0741\overline{\sigma})]^{5.98} \exp\left(\frac{-39,600}{T + 273}\right)$$ [29]

where,

$$\text{for } T > \text{Ar}_3, \quad A_0 = 4.2 \times 10^9$$

$$\text{for } T < \text{Ar}_1, \quad A_0 = 4.2 \times 10^{12}$$

and Ar_1 and Ar_3 were 650 °C and 780 °C, respectively.

The original equation was based on tensile data for 0.051 pct C austenite at 0.2 pct plastic strain. The plastic-creep strain rate was enhanced by a factor of 1000 for temperatures extrapolated below the Ar_1 into the ferrite/pearlite region. Within the two-phase region, a weighted average of the two plastic creep rates was employed, based on the volume fractions of austenite and ferrite/pearlite present. Figure 3 shows the strain-rate temperature curves generated on the basis of Eq. [29] and employed in the model.

A test simulation was also conducted using a relationship by Sakui and Sakai[29] for secondary creep that was reported by Grill and Schwerdtfeger[3] to underpredict bulging strain in continuous casting bulging studies:

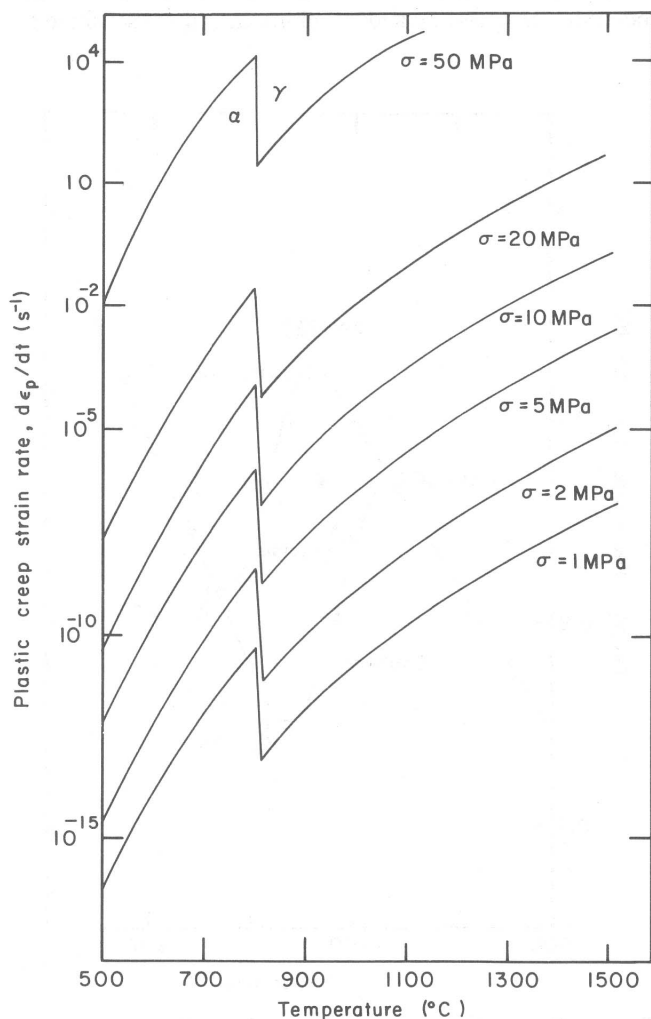$$\dot{\varepsilon}_p = 4\overline{\sigma}^{5.4} \exp\left(\frac{-34,470}{T + 273}\right)$$ [30]

B. Thermal Linear Expansion Function

Coefficients for thermal linear contraction of iron are 2.2×10^{-5} m/m °C for austenite and 1.55×10^{-5} m/m °C for ferrite.[20,36] These values are fairly independent of both composition and temperature above 300 °C. However, one of the most important sources of stress that could potentially cause panel cracking is the volume change which accompanies the phase transformation from austenite to ferrite between the A_3 and A_1 temperatures. The expansion on cooling is 0.342 pct[11,20] which is equivalent to a temperature change over 150 °C, as illustrated in Figure 4. This figure also shows the 0.20 pct contraction that accompanies the delta to austenite transformation at 1400 °C.[20] Above the solidus temperature, the model assumes TLE to remain constant in order to help prevent stress development in the liquid.

Modifications of this *TLE* function for steel were made difficult by the complexities of the $\gamma \rightleftarrows \alpha$ phase transformation, which occurs over a range of temperatures and depends on both composition and thermal history. It was accomplished as follows. First, a relationship was derived, using literature data and dilatometer experiments, to include the influence of carbon content on the percent linear change accompanying the $\gamma \rightleftarrows \alpha$ phase transformation:[19]

$$TLE(\gamma \rightarrow \alpha @ 900 °C)$$
$$= 0.342 \text{ pct} - 0.278 \text{ pct(pct C)}$$ [31]

Then it was assumed that the overall *TLE* value could be calculated using a weighted average of *TLE* for the volume fractions of ferrite/pearlite and austenite phases present:

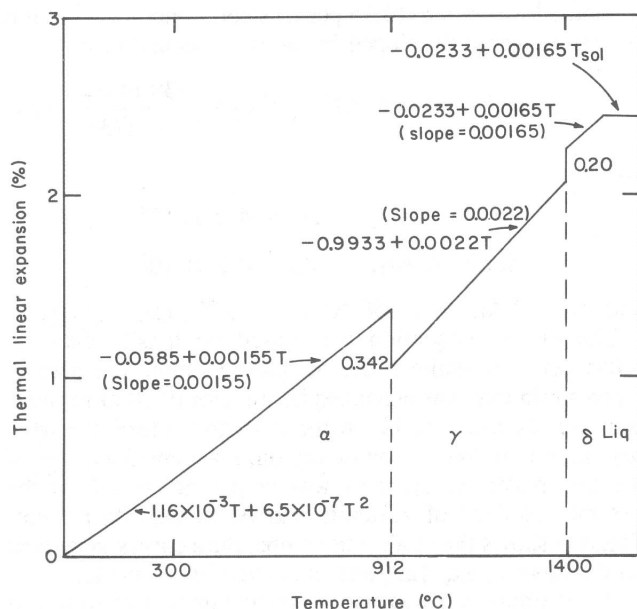$$TLE = \frac{(\text{pct } \alpha)}{100}(TLE_\alpha) + \frac{(\text{pct } \gamma)}{100}(TLE_\gamma)$$ [32]

Fig. 4—Thermal linear expansion of iron assumed in stress model.

where TLE_α and TLE_γ are based on the empirical equations in Figure 4, modified to include Eq. [32].

If the structure present was dependent only on temperature, it would now be a simple matter to use the Fe-C phase diagram to calculate the equilibrium fractions of ferrite and austenite present at any temperature between the A_3 and A_1. However, even at the slow cooling rates present in the ingot, there is an unavoidable delay in nucleation before the start of the transformation which gives rise to a temperature difference between Ar$_3$ and Ac$_3$ of about 60 °C. Ignoring this effect would produce a qualitative difference in stress generation. For example, reheating a portion of the ingot that had cooled into the two-phase region will initially result in expansion. However, an equilibrium model basing volume on temperature alone would incorrectly model this situation as a contraction. In addition, the reversal from cooling to heating that occurs upon charging to the soaking pit produces a hysteresis effect in TLE that is instrumental in developing the phase transformation stresses that result in panel cracking. Thus, it was necessary to include phase transformation kinetics in the model. This was done by incorporating Continuous-Cooling Transformation, CCT, data into equations employed to calculate the fraction austenite present as a function of temperature in the two-phase region as given below:

Ar$_1$ < T < Ar$_3$, cooling:

$$\text{pct } \gamma = 50 \cos\left[\pi \frac{(\text{Ar}_3 - T)}{(\text{Ar}_3 - \text{Ar}_1)}\right] + 50 \qquad [33]$$

Ac$_1$ < T < Ac$_3$, heating:

$$\text{pct } \gamma = 50 \cos\left[\pi \frac{(\text{Ac}_3 - T)}{(\text{Ac}_3 - \text{Ac}_1)}\right] + 50 \qquad [34]$$

For the slow cooling rates present in the ingot, the CCT curves are relatively flat so that the transformation is better characterized by start and finish temperatures than by times. The model therefore requires, as input, the $\gamma \rightarrow \alpha$ phase transformation temperatures for both cooling (Ar$_3$, Ar$_1$) and heating (Ac$_3$, Ac$_1$). Since data in this form are readily available for most alloys of steel, the model is capable of simulating any desired steel composition with ease.

The transformation fractions generated using the simple cosine relations in Eqs. [33] and [34] produce S curves for fraction *vs* time that are remarkably close to those found experimentally.[19] When reheating a partially transformed structure, the austenite fraction is assumed to remain constant until the heating equation, Eq. [34], generates larger austenite fractions. To accomplish this, the model must track the heating/cooling state of each node. The result more closely simulates the true expansion/contraction behavior of steels subject to varying thermal treatments than has been attained in previous stress models. An example of thermal linear expansion *vs* temperature curves produced using this novel approach is given in Figure 5 for continuous cooling and heating. This figure also presents the transformation temperatures employed to simulate the typical low-carbon steel, chosen in Part I because of its susceptibility to off-corner panel cracks.

C. *Elastic Modulus*

The elastic modulus of steel decreases significantly with increasing temperature and, in addition, is quite sensitive to
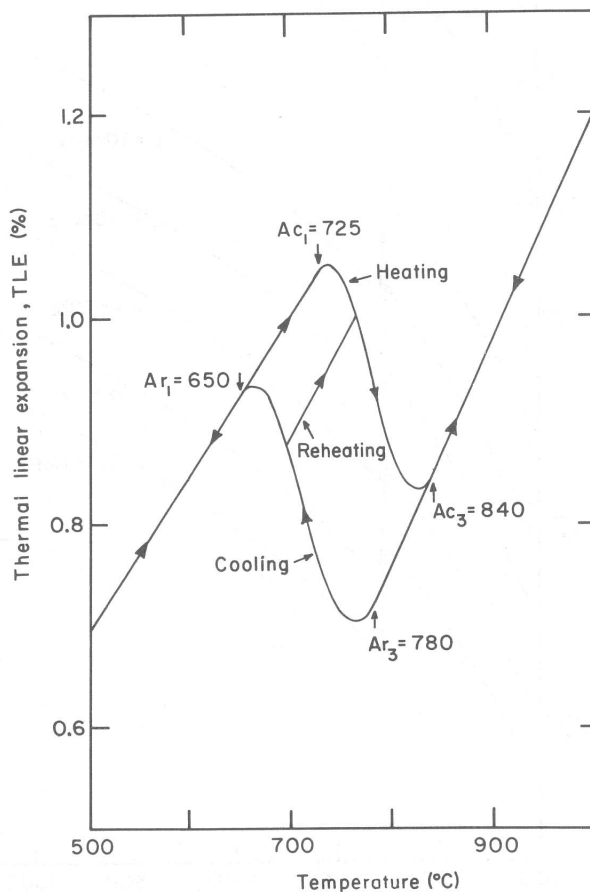

Fig. 5—Thermal linear expansion curves for cooling and heating of low-carbon steel used in the model.

the strain rate at which measurements are made. This phenomenon can be incorporated into the stress model in two different ways. If strain rate during processing remains relatively constant, stress-strain data measured at the appropriate strain rate can be employed and creep can be ignored. Alternatively, unrelaxed elastic modulus data can be employed, when strain rate is extremely variable, and creep can be accounted for separately with a time-dependent, elasto-viscoplastic function.

Figure 6 presents the different elastic modulus functions used in the model. The relaxed data of Puhringer[37] has the advantage of gradually tending to almost zero at the liquidus temperature, which helps to avoid numerical difficulties in the computation. The function in Figure 6 obtained from "unrelaxed" data[20,38–41] is considerably higher at temperatures above 768 °C and tends toward a finite elastic modulus of about 25 pct of the room temperature value as the solidus temperature is approached.[20]

Note that austenite has an elastic modulus of 15 to 20 GPa higher than α or δ iron at the same temperature. Effects of alloying elements on elastic modulus were ignored since they are known to be quite small.[41] Above the solidus temperature, the elastic modulus was drastically reduced to only 1 MPa in order to ensure no resistance to strain by the liquid.

V. STRESS MODEL VERIFICATION

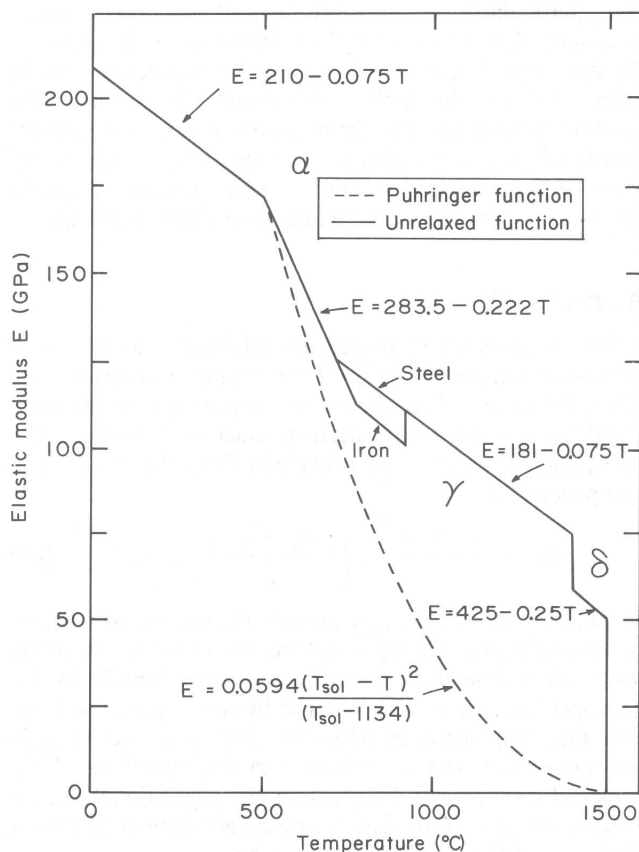To verify that the stress model had been formulated and programmed correctly, it was first employed to solve two simple problems whose solutions could be found analytically.

A. First Test Problem

To verify the basic load-deflection calculation, the model was first run to predict the tip deflection for an isothermal, statically loaded, $0.1 \times 1.2 \times 4.8$ m cantilever beam with a 400 N/m parabolic shear load distribution at the tip. A constant elastic modulus of 300,000 MPa and Poisson ratio of 0.25 were assumed. The problem is illustrated in Figure 7(a). From beam theory, the horizontal deflection at the tip is 0.035583 m and the axial stress at point A is 600 MPa.

The stress model was run for one time step under plane stress conditions using the 165 node mesh shown in Figure 7(b) which, due to symmetry, models only one-half of the beam and sets horizontal displacement along the centerline to zero. The results were 0.0337 m tip deflection (5.3 pct low) and 537 MPa at point A (10.7 pct low) which are within engineering accuracy and are consistent with the inherent stiffness of constant-strain triangles. Either further mesh size reduction or extra "time steps" using the out-of-balance force vector as a driving force could be utilized to reduce the error to any desired lower level.
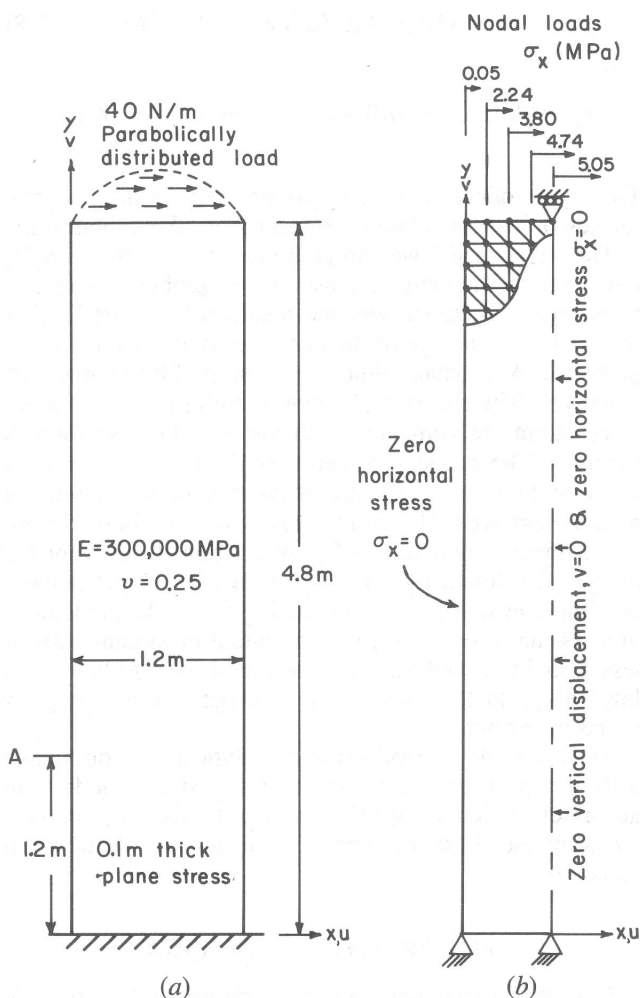

Fig. 6—Elastic modulus functions used in stress model.

Fig. 7—First test problem for stress model verification: (a) schematic diagram and (b) finite-element mesh.

B. *Second Test Problem*

A second analytical solution was obtained for a problem involving both thermal strain and creep to verify these aspects of the stress model. The same long, thin beam used in the first problem was left unconstrained for this analysis. From an initial uniform temperature of 0 °C, the beam was subjected to an instantaneous, one-dimensional, parabolic temperature distribution across its width:

$$T = -25 + 208.3x^2 \qquad [35]$$

This function was chosen because there is no net change in length of the beam due to thermal expansion (*i.e.*, $v = 0$) and the same simple expression for the initial stress-distribution in the y direction, σ_y, exists throughout the beam.

The initial solution was taken from Boley and Weiner[42] and assuming an elastic modulus of 100,000 MPa, thermal expansion coefficient of 2×10^{-5} °C^{-1} and Poisson ratio of 0.3, yields:

$$\sigma_y = -E\alpha T = 50 - 416.6x^2 \qquad [36]$$

The beam was subsequently allowed to relax according to the relation:

$$\dot{\varepsilon}_p = 4.0 \times 10^{-8}\sigma \qquad [37]$$

The solution to this time dependent problem is:

$$\sigma_y = (50 - 416.6x^2)\exp(-0.004t) \qquad [38]$$

and

$$\varepsilon_p = (0.0005 - 0.00416x^2)[1 - \exp(-0.004t)] \qquad [39]$$

The asymptotical increase in plastic-creep strain gradually relaxes σ_y to zero while σ_x remains zero throughout time.

The stress model was programmed to solve this simple, transient, thermal-stress, plastic-creep problem using the plane-stress, finite-element mesh shown in Figure 8. This mesh takes advantage of the one-dimensional nature of the problem. A constant time-step size of 30 seconds was employed. The model predictions of both stress and plastic-creep strain are compared with the analytical solution in Figure 9. The surface and center of the beam are the least accurate locations from the standpoint of the numerical model, and were therefore singled out for comparison. Stress model predictions of plastic strain differ from the analytical solution by a maximum of only 15 pct initially and improve steadily with increasing time. The predictions of stress are even closer, with an initial maximum error of less than 5 pct, and this decreases until the absolute stress level drops to the same order of magnitude as computer round-off errors.

The favorable comparison with analytical solutions to two different problems indicates that the stress model can accurately calculate displacement, strains, and stresses including the effects of thermal expansion and plastic-creep relaxation.

VI. FRACTURE CRITERIA

Comprehensive data on temperature and strain-rate dependent ultimate strength and fracture strain are not avail-
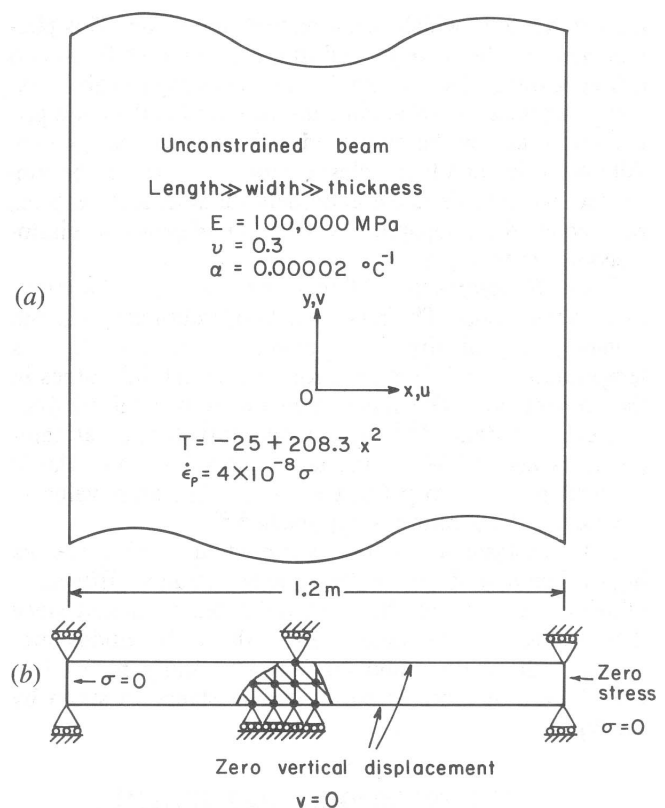

Fig. 8—Second test problem for stress model verification: (*a*) schematic diagram and (*b*) finite-element mesh.

able, particularly for the varied thermal and stress histories encountered at various locations in the ingot. In addition, the data, obtained in one dimensional tensile tests, must be interpreted for the multi-dimensional stress-strain state existing in the ingot. For the purposes of presenting sample results of the stress model predictions in the present paper, plots of three separate variables were constructed on the ingot cross section at selected times during processing.

A. *Principal Stresses*

For materials susceptible to brittle failure, the criterion of maximum normal stress has been found to be effective.[43] Thus, the magnitude of the maximum principal tensile stress should give a good indication of cracking tendency. The two principal stresses are calculated from the three stress components by:

$$\sigma_{I,II} = \frac{\sigma_x + \sigma_y}{2} \pm \left[\left(\frac{\sigma_x - \sigma_y}{2}\right)^2 + \tau_{xy}^2\right]^{1/2} \qquad [40]$$

In addition, the columnar grain boundaries, extending perpendicularly from the ingot surface, are known to be weak, so the orientation of the stresses is also important. Thus, the principal stresses were calculated by the stress model and presented graphically as stress bars plotted at each node in the mesh. The bars are oriented in the directions of the principal stresses with lengths that are proportional to their magnitudes, and compressive stresses are distinguished with tic marks at the end of each stress bar.
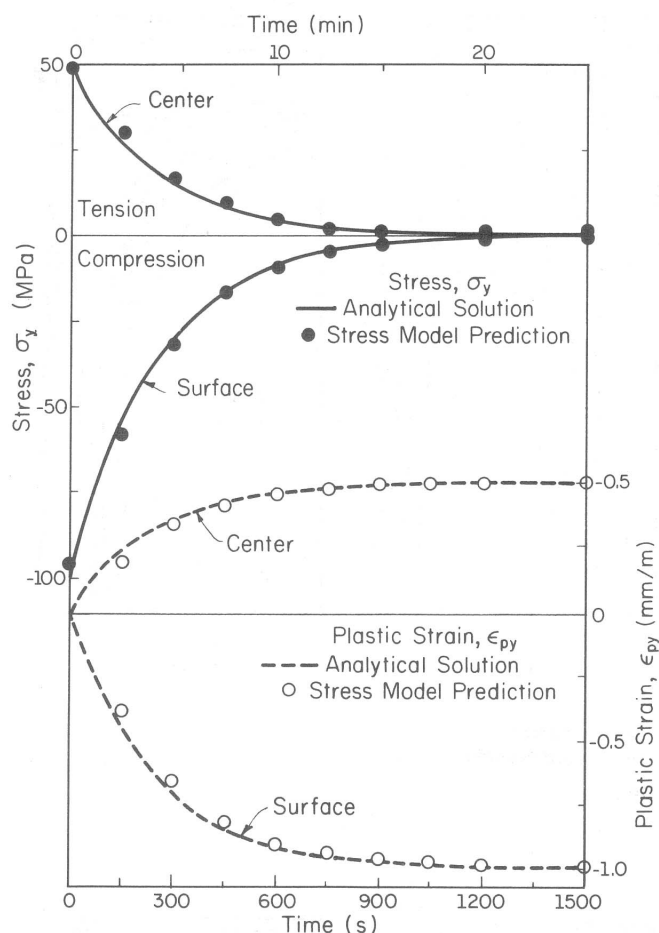
Fig. 9 — Comparison of analytical and numerical predictions of stress and strain for second test problem.

B. *Effective Stress*

For materials that fail in a ductile manner, other fracture criteria are based on the maximum shearing stress (Tresca) or the maximum distortion energy (Von Mises).[43] The latter criterion states that failure will occur when the effective stress, as defined by

$$\overline{\sigma} = (\sigma_x^2 + \sigma_y^2 + 3\tau_{xy}^2 - \sigma_x\sigma_y)^{1/2} \qquad [41]$$

exceeds the ultimate strength. The effective stress, $\overline{\sigma}$, has already been calculated by the model and employed as a scalar stress value to determine the plastic creep strain from the three stress components.

Regardless of their cause, cracks can propagate and open up only under tension. Thus, to distinguish regions of tension and compression, the parameter, $\overline{\sigma}$, was assigned a negative value if the principal stress with the largest magnitude was compressive. The effective stress distribution is displayed graphically as iso-stress contour lines.

C. *Plastic-Creep Strain*

The final fracture criterion that is most often utilized involves a limit on either the plastic strain or the total strain. Because the total strain is largely composed of thermal strain, which should not bear any direct influence on cracking tendency, this criterion was rejected. Plastic strain,

however, should be an effective fracture criterion. For a grain-boundary void coalescence fracture mechanism, both tensile and shear plastic strains contribute to the structural damage ultimately leading to failure. Thus the increments of plastic-creep strain already calculated in the model using Eq. [21] were accumulated in a positive sense by

$$\overline{\varepsilon}_{\mathbf{p}_{t+\Delta t}} = \overline{\varepsilon}_{\mathbf{p}_t} + |\Delta t \dot{\varepsilon}_{\mathbf{p}}| \qquad [42]$$

Contour plots of plastic-creep strain so calculated are then presented in the same manner as effective stress, in order to portray the strain state of the ingot.

VII. RESULTS

Figure 10 presents the principal stresses and effective stresses that arise during the processing of a 760 mm × 1520 mm, 23,000-kg, low-carbon steel ingot. The model simulation was based on temperatures generated by the heat-flow model. These temperature results were presented in Part I,[10] which also gives details of the mesh geometry, steel composition, and processing conditions under which this simulation was conducted.

Figure 10(a) shows that, at the end of a four-hour cooling period in the mold, the entire surface of the ingot is in slight compression (as indicated by tic marks at the ends of the stress bars) while the interior beneath this region is in slight tension. This stress reversal occurs because at the beginning of solidification, the thin shell is relatively free to contract around the liquid core. As the shell thickens, the cooling rate at the surface decreases and there may even be reheating. This forces the surface layer into compression and sets up complementary tensile stresses just beneath the surface. Figure 10(a) shows that the greatest stresses are compressive and are found in the vicinity of the corner. This compression arises from the expansion accompanying the prolonged reheating at the corner and the beginning of transformation from austenite to ferrite. Stresses in the interior are small both because of the low temperature gradients and the high temperatures which produce lower elastic modulus values and rapid stress relaxation by plastic creep.

After cooling for 4 hours in the mold, the ingot is stripped. It is then allowed to cool for 1.75 hours in air before it is charged into a soaking pit. Upon stripping, the rapid contraction of the chilled ingot surface produces tension over the majority of the wide face as shown in Figure 10(b), where the time after stripping is 10 minutes. However, the surface layer quickly cools into the two-phase region between the Ar_3 and Ar_1 temperatures, and the expansion accompanying transformation forces the surface back into compression, where it remains for several hours.

As the two-phase region moves deeper into the ingot, the associated compressive stresses also move deeper and increase in magnitude. They induce complementary tensile stresses in the region just ahead of the compressive band. As shown in Figure 10(c)(i), the principal tensile stresses of this interior region of tension are oriented primarily in a radial direction, roughly parallel to the grain boundaries. This contrasts with the compressive band whose greatest principal stress lies tangential to the surface as an internal "hoop stress". Once the ingot surface falls below the Ar_1 temperature, a trailing tensile wave is produced as the fully transformed steel contracts with further cooling of the
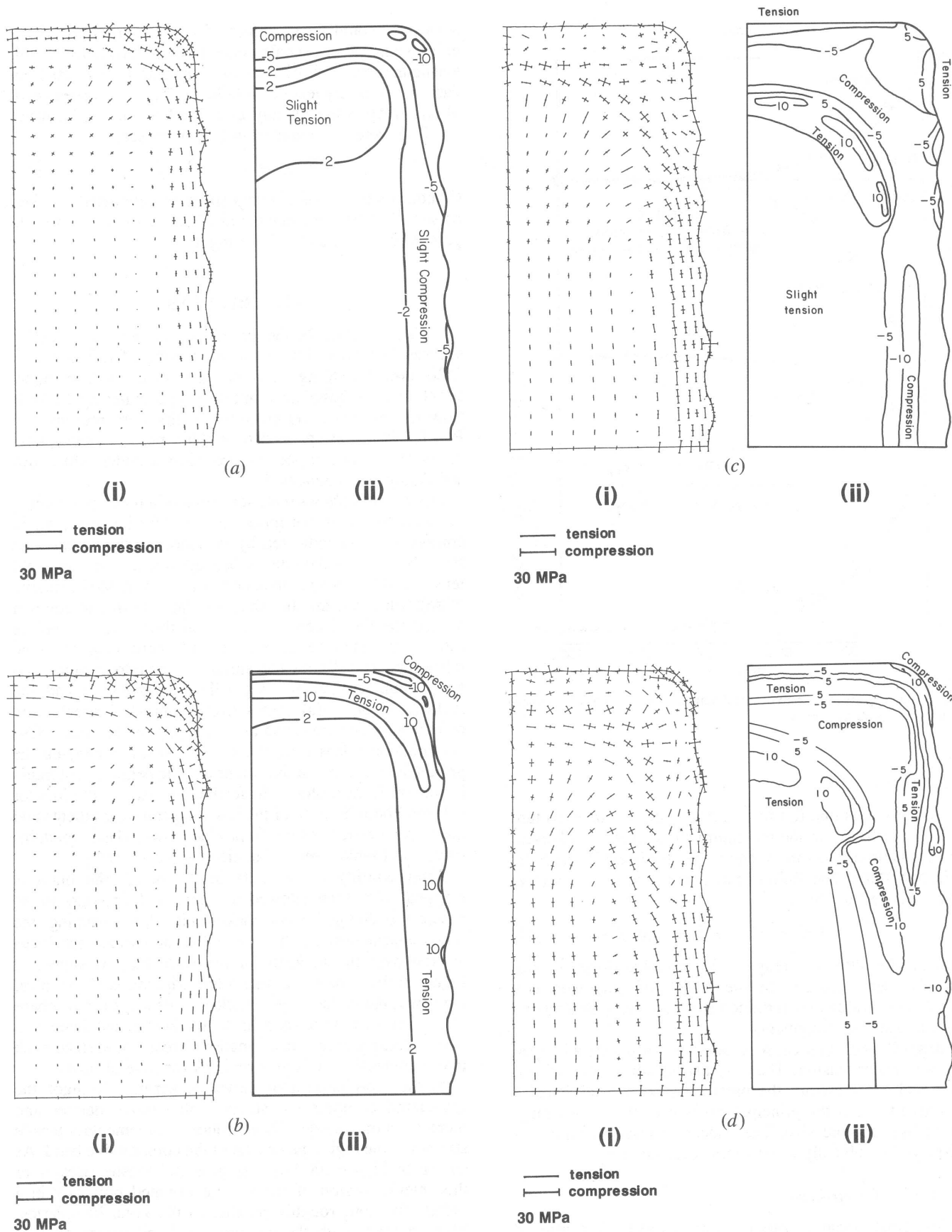
Fig. 10—Principal stresses (i) and effective stress contours (MPa) (ii) calculated by stress model for simulated processing of 760 × 1520 mm, low-carbon steel ingot. (a) Stress state at conclusion of 4 h cooling in the mold (14,400 s). (b) Stress state during air cooling, 10 min after stripping from the mold (15,000 s). (c) Stress state at conclusion of 1.75 h air cooling (20,700 s). (d) Stress state during reheating, 20 min after charging to soaking pit (21,900 s). (e) Stress state during reheating, 70 min after charging to soaking pit (24,900 s). (f) Stress state during reheating, 5 h after charging to soaking pit (38,700 s). (g) Stress state during air cooling, 15 min after drawing from pit (70,900 s).
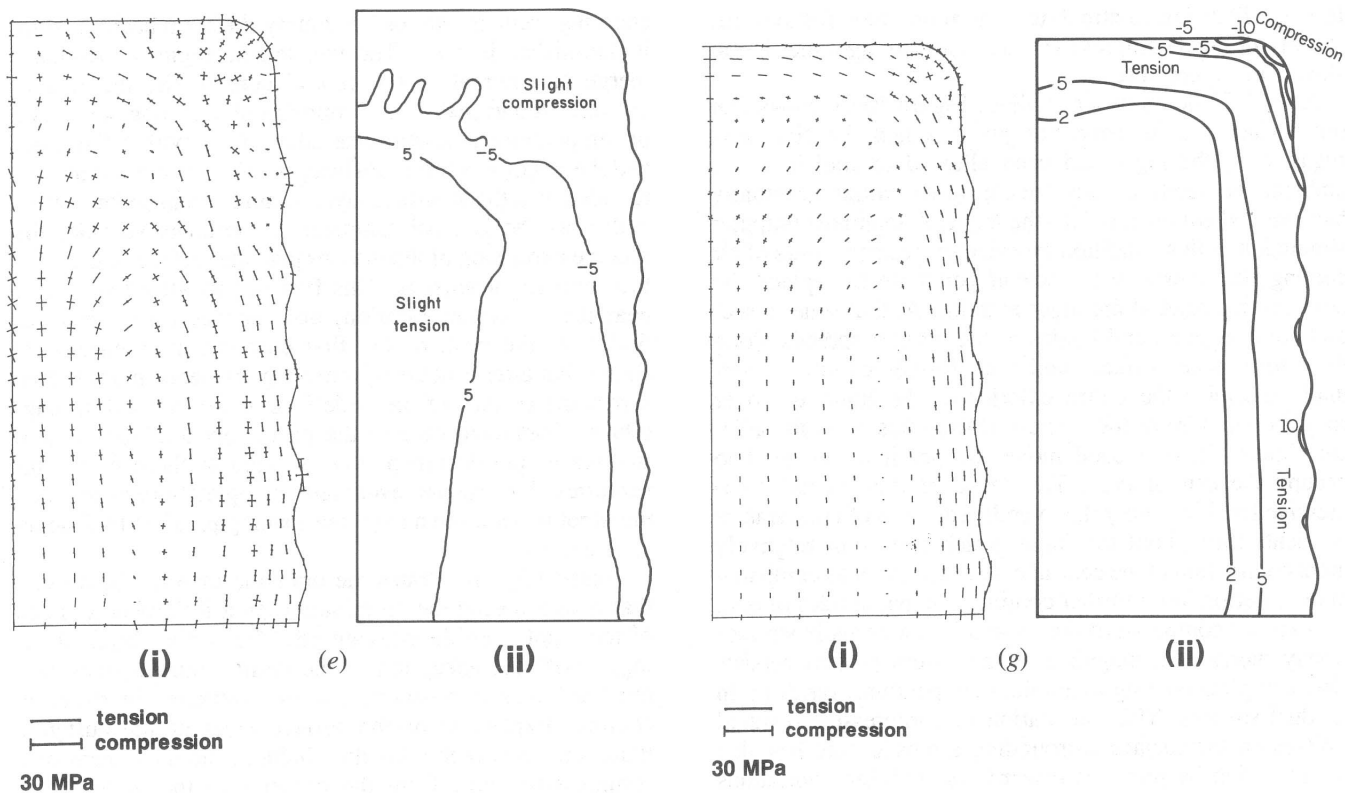
(i) (e) **(ii)**

Slight compression

Slight tension

— tension
⊢——⊣ compression

30 MPa

(i) (g) **(ii)**

Compression

Tension

Tension

— tension
⊢——⊣ compression

30 MPa

(i) (f) **(ii)**

Slight tension

Slight tension

— tension
⊢——⊣ compression

30 MPa

Fig. 10 Cont. — Principal stresses (i) and effective stress contours (MPa) (ii) calculated by stress model for simulated processing of 760 × 1520 mm, low-carbon steel ingot. (a) Stress state at conclusion of 4 h cooling in the mold (14,400 s). (b) Stress state during air cooling, 10 min after stripping from the mold (15,000 s). (c) Stress state at conclusion of 1.75 h air cooling (20,700 s). (d) Stress state during reheating, 20 min after charging to soaking pit (21,900 s). (e) Stress state during reheating, 70 min after charging to soaking pit (24,900 s). (f) Stress state during reheating, 5 h after charging to soaking pit (38,700 s). (g) Stress state during air cooling, 15 min after drawing from pit (70,900 s).

ferrite. This less-distinct tensile zone then follows the sharply-defined compressive wave into the ingot interior, as shown in Figure 10(d).

After 1.75 hours of air cooling, Figure 10(c) shows that the surface tensile zone has just reached the first corrugation. If the ingot had been allowed to cool in air to ambient temperature, this tensile wave would eventually have moved completely into the ingot. A separate computer simulation of this condition revealed that after 5 hours of air cooling, the tensile wave would penetrate to replace the compressive band at the ingot exterior. At that time, a second compressive band begins at the corner, spreads along the narrow-face surface, and with further cooling, eventually occupies the entire exterior of the ingot to cover roughly one-third of the section. During this time, the adjacent interior tensile band moves deeper into the ingot to occupy the central core. The cause of this second compressive band is simply the overall reduction of temperature gradients throughout the ingot which results in relatively more contraction in the central core of the ingot as compared to the exterior. With further cooling, the magnitudes of both the exterior compressive region and interior tensile stresses slowly increase in magnitude. This stress pattern persists after complete cooling to ambient temperature, resulting in residual stresses. This calculation of compressive residual stresses on the surface surrounding a tensile core has also been verified by previous researchers studying continuous casting of cylindrical sections.[1]

If instead of complete air cooling, the ingot is processed according to the conditions outlined in Part I,[10] it is charged into the soaking pit following 1.75 hours of cooling in air. Figures 10(d) and (e) then illustrate the dramatic changes in the stress pattern that occur as the internal pit temperature increases from 1000 °C initially to a soaking temperature of 1200 °C. The most interesting feature is the development of a temporary tensile region beneath the ingot surface in the vicinity of the corner and the first corrugation. The location and shape of this zone corresponds closely to the eventual location of off-corner panel cracks.

This tensile zone initiates on the surface at the center of the wide-face almost immediately after charging. It then moves below the ingot surface as it migrates toward the corner. After 20 minutes, the same zone has moved completely below the ingot surface and has extended around the corner to lie beneath the narrow face as well (Figure 10(d)). The maximum tensile stress is nearly 10 MPa and is centered beneath the trough between the first and second corrugations. With further heating, the zone moves deeper into the ingot and diminishes in both size and magnitude. It is replaced by compression at the exterior of the ingot, as shown in Figure 10(e), after 70 minutes of reheating.

This tensile region is a direct result of the "wrapping" movement of the Ac_3 temperature isotherm noted in Part I.[10] It arises because the ferrite/pearlite mixture in the subsurface zone is contracting during retransformation to austenite while it is enclosed by untransformed austenite that is expanding. Figure 10(d) shows that the tensile stresses in this zone are biaxial, but have components oriented perpendicular to the grain boundaries.

The other major tensile region, that was located on the inside of the two-phase compressive band at the time of charging, remains almost stationary during reheating while it diminishes in area. The two tensile regions eventually merge and retreat to the central core of the ingot. Figure 10(e) shows that after 70 minutes of reheating, a reversal of temperature gradients has taken place within the ingot and the result is a large, diffuse, interior tensile region surrounded by a thick surface layer in mild compression. Eventually, as the internal temperature gradients subside, the relative expansion of the interior puts the surface of the wide face into slight tension. This first occurs after two hours, near the off-corner location, and reaches a maximum of 6 MPa at the peak of the first corrugation. Figure 10(f) shows that after 5 hours of reheating this tension has spread across the surface of the wide face and decreased in magnitude. Continued time in the pit merely diminishes these stresses as plastic creep flow is rapid at these high temperatures. Stresses are eventually completely relaxed when the ingot is withdrawn from the soaking pit after 13.7 hours of reheating.

Figure 10(g) illustrates the dramatic increase in stresses that occurs during the 15-minute period following removal of the ingot from the soaking pit. The surface layer of the ingot, with the exception of the corner, immediately goes into tension as the austenite exterior contracts with the rapid cooling. Expansion of the surface layer as the austenite transforms below the Ar_3 then induces the movement of a compressive wave from the corner into the ingot. After 30 minutes, the entire surface of the ingot is in compression. Further cooling produces stress development that is qualitatively very similar to that arising during air cooling after stripping from the mold.

It is evident from the discussion of Figure 10 that the description of stress development based on principal stress results is consistent with that portrayed by the effective stress contours. Significant differences in magnitude between $\bar{\sigma}$ and the larger of σ_I and σ_{II} arise only when the two principal stresses are nearly equal in magnitude but opposite in sense, which indicates a region of higher shear.

Figure 11 presents contours of accumulated plastic-creep strain at several important times during ingot processing identified in the previous discussion. The overall strain pattern that develops by the time of stripping (Figure 11(a)) remains essentially unchanged thereafter. Significant strain arises while the ingot is in the mold because temperatures are so high and the rapid cooling induces large volume changes. However, a good deal of plastic deformation also occurs during air cooling, particularly at the ingot surface where the compressive zone develops. A comparison of Figures 11(b) and (c) shows that during the first hour of reheating, when the most dramatic changes in stress pattern take place, the plastic-creep strain contours change very little. Plastic-creep strain remains highest at the center of the surfaces of the wide faces and narrow faces until the latter stages of reheating when creep strain builds up at the corner under compression.

The most notable feature is that maximum plastic-creep strain rarely exceeds 5 pct anywhere in the ingot. At the eventual location of panel cracks, beneath the first corrugation, plastic strain remains below 2 pct even after many hours of reheating. This result reveals the importance of temperature-dependent metallurgical factors in the fracture
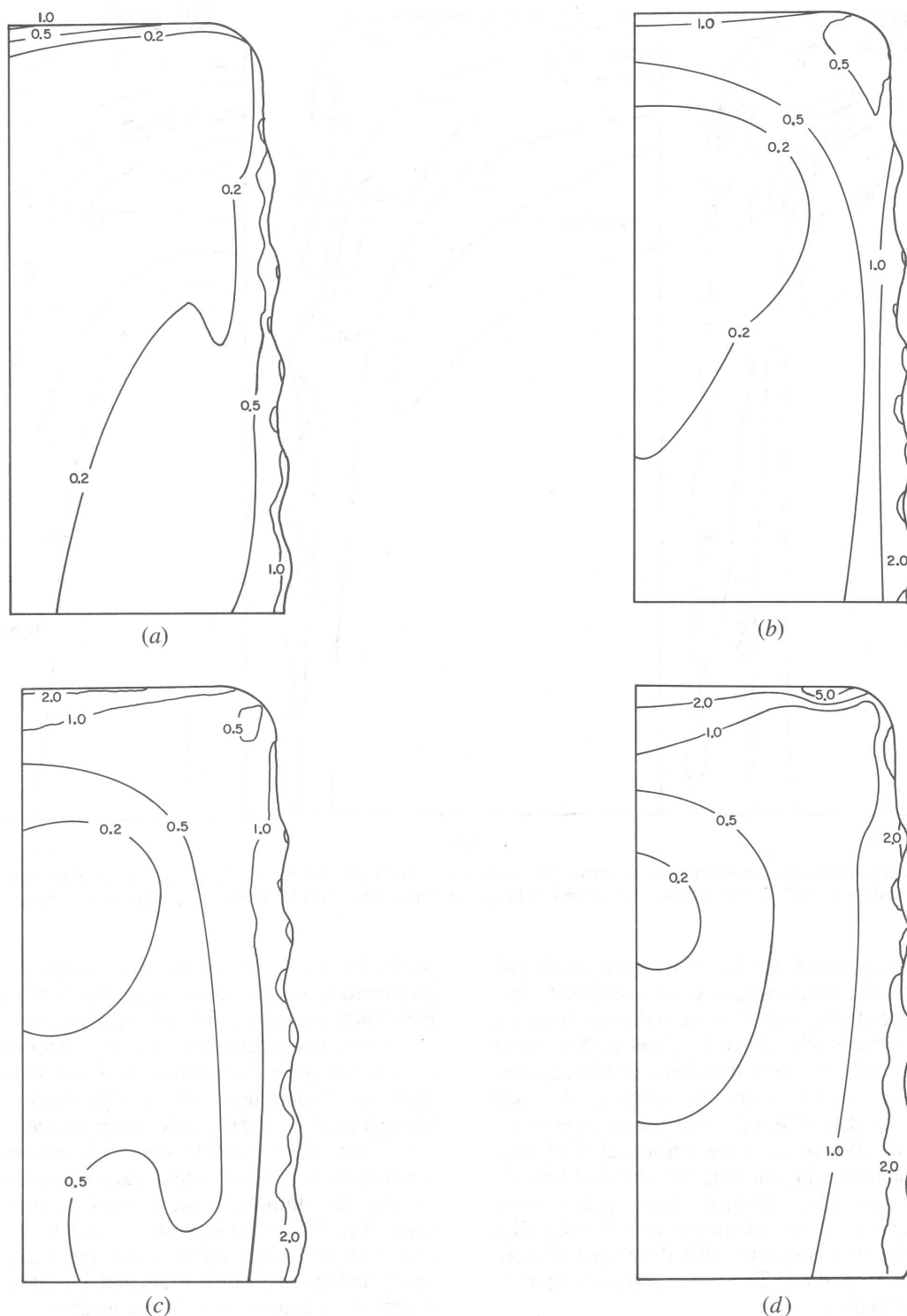
Fig. 11 — Accumulated plastic-creep strain contours (pct) calculated by stress model for simulated processing of 760 × 1520 mm, low-carbon steel ingot. (a) Strain state at conclusion of 4 h cooling in mold (14,400 s). (b) Strain state at conclusion of 1.75 h air cooling (20,700 s). (c) Strain state during reheating, 100 min after charge (24,300 s). (d) Strain state during reheating, 5 h after charge (38,700 s).

mechanism. Crack formation is not possible without a significant loss of ductility arising from grain boundary embrittlement or local strain concentration. Plastic-creep strain rates calculated from these results range from 1×10^{-9} to 4×10^{-6} s^{-1} at the surface and average about 3×10^{-7} s^{-1}.

VIII. EFFECT OF MECHANICAL PROPERTY DATA

Test runs of the stress model were conducted to determine the influence of the mechanical property data employed. In
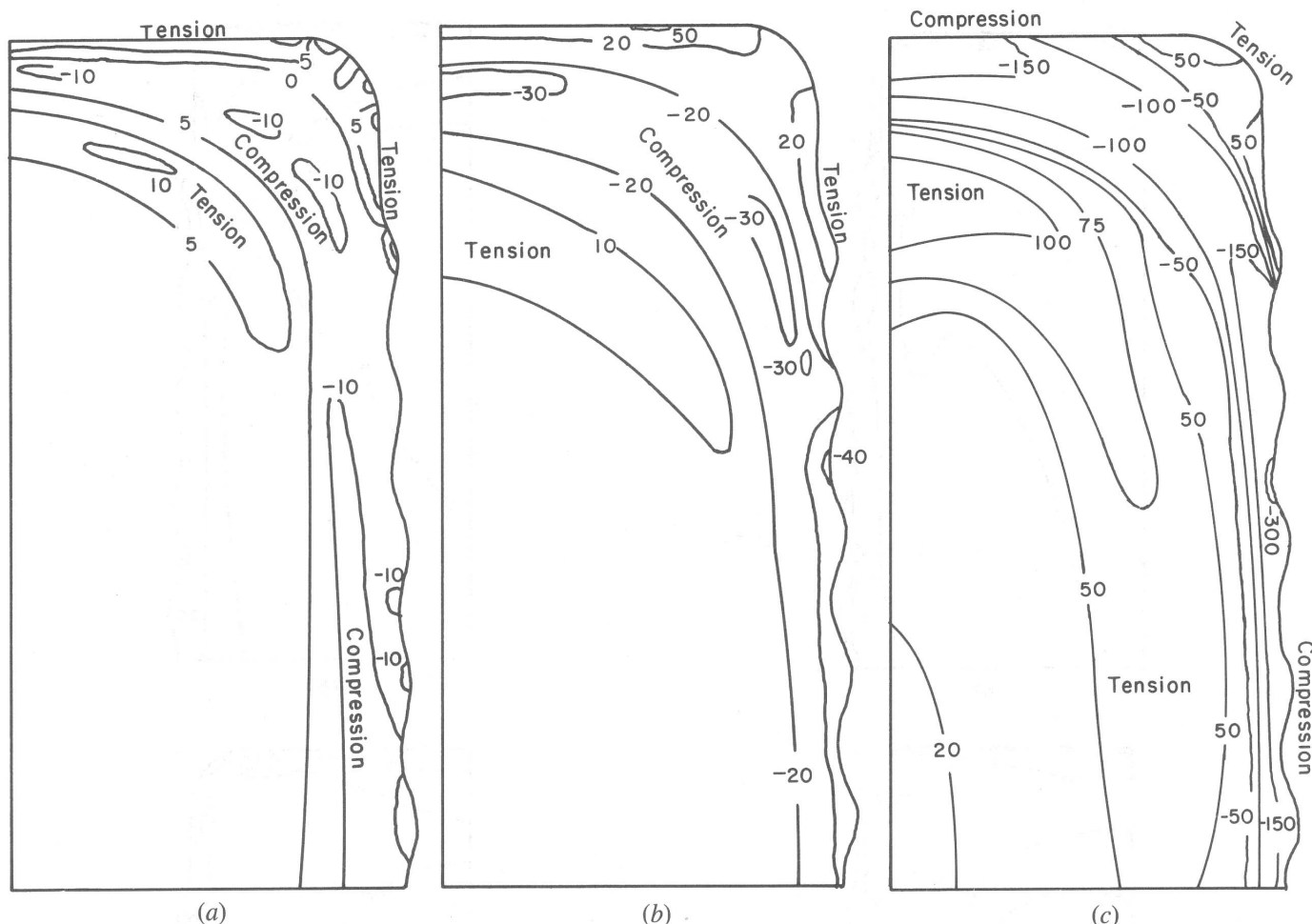
Fig. 12—Influence of creep function on effective stress contour distribution at 18,900 s (air cooling, 1.25 h after strip). (a) High plastic-creep strain rate (Wray data for low-carbon steel).[20] (b) Low plastic-creep strain rate (Sakui and Sakai data).[29] (c) No plastic creep (elastic calculation).

particular, the importance of the function employed for calculating visco-plastic strain rates was demonstrated. Figure 12 presents the effective stress contour distributions that developed after 4 hours of mold cooling and 1.25 hours of air cooling using three different functions for plastic-creep strain rate. Figure 12(a) presents the results of the final simulation using the data of Wray[20] with plastic-creep strain rate accelerated by 1000 times in the ferrite, Eq. [29]. Figure 12(b) was obtained using the data of Sakui and Sakai,[29] whose function, Eq. [30], produces lower plastic-creep strain rates for a given stress and temperature. Finally, Figure 12(c) presents the distribution that developed without including plastic-creep at all. This corresponds to a purely elastic stress distribution.

In general, a reduced plastic-creep rate simply results in increased stress levels in the peak stress zones such as the band of high compression. However, important qualitative differences also are apparent. Both the compressive band and internal tensile band tend to occur deeper in the ingot with decreasing plastic-creep rate. The consequences of ignoring plastic-creep completely are severe. During a sequence of alternating compression and tension, the initial compressive peak is an order of magnitude lower than would actually be encountered. Subsequent tensile peaks must first overcome this artificial compression which results in tensile

peaks that are lower, on a relative level, than found when plastic-creep was included. Secondly, while not apparent in the figures presented, the lack of plastic-creep changes the subsurface stress pattern from principal tensile stresses parallel to the grain boundaries, to hoop stresses normal to them. In addition, unreasonably high tensile stresses arise in the ingot center when plastic-creep relaxation does not occur. Figure 12(c) exhibits stresses in excess of 300 MPa, which at the high temperature and low strain rates involved, exceeds the ultimate tensile strength by over 10 times. Finally, it is difficult to estimate accurately the strains generated with an elastic model since the elastic strain alone vastly underpredicts total strain and the entire thermal strain overpredicts deformation. These results clearly indicate the necessity for adequately including strain-rate and temperature dependent, plastic-creep in the stress model.

The processing of higher carbon steel was simulated using a plastic-creep function, Eq. [28], that, unlike Eq. [29], included no acceleration of plastic-creep rate in the ferrite + pearlite region below the Ar_1. The effect of this change in steel composition on the resulting stress pattern can be seen by comparing Figure 12(a) with Figure 13. The most important difference is the increased level of tensile stress in the regions associated with contracting ferrite + pearlite. This occurs because the plastic-creep relaxation
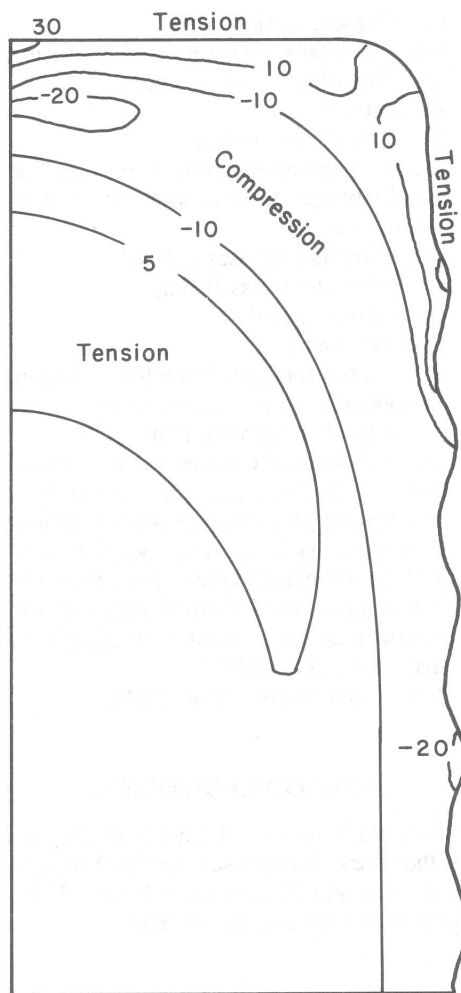
Fig. 13—Effective stress contour distribution at 18,900 s during air cooling, 1.25 h after strip, calculated using property data for medium-carbon steel.

Fig. 14—Maximum principal tensile stress contours at 18,900 s during air cooling, 1.25 h after strip, calculated assuming no creep.

rate in the ferrite/pearlite phase of higher carbon steels is not enhanced over that in austenite. In addition, the internal tensile zone occurs deeper in the ingot.

An interesting feature of the stress pattern development near the vicinity of the corrugations can be seen in Figure 14. The maximum tensile stresses occur in roughly circular zones centered directly beneath each corrugation peak. This feature, which was generally present in all of the simulations, is most clearly evident in the elastic model results, where local stress variations are magnified relative to the full plastic model simulations.

The choice of elastic modulus function was found to have little effect on the development of the major stresses associated with the phase transformation zone. Only at high temperatures, near the solidus, did the simulation with the higher unrelaxed elastic modulus function produce stresses of significantly increased magnitude. Smaller time steps were required to handle the increased numerical difficulties associated with the unrelaxed function. Although this was not of great concern for the present study which focused on the intermediate temperatures associated with panel crack formation, it may be of importance to continuous casting, where stresses at temperatures near the solidus can be responsible for hot-tearing cracks.
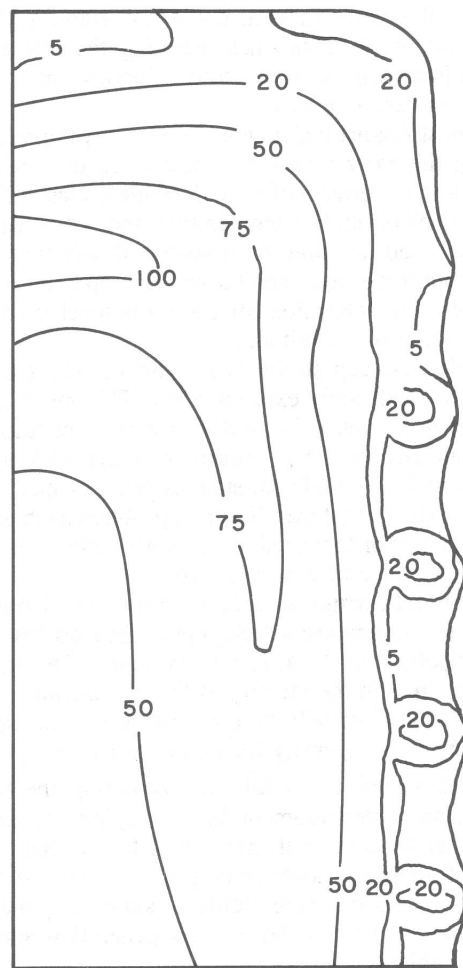
IX. CONCLUSIONS

An accurate, sophisticated, but cost-effective, mathematical stress model has been developed to calculate two-dimensional stress and strain development in a steel ingot during thermal processing. The model uses, as input, temperatures calculated by an uncoupled heat-transfer model that includes the effects of irregular geometry such as rounded corners and mold corrugations.

The ability of the stress model to accurately calculate displacement, strain and stress, including the presence of thermal loading and time-dependent plastic flow, was demonstrated through comparison against analytical solutions. The model was then used to calculate stress and plastic-creep strain contours in a transverse slice at mid-height of a 760 × 1520 mm, low-carbon steel ingot processed under conditions conducive to panel crack formation. From the results of these simulations, the following conclusions can be drawn:

1. The development of major regions of tensile and compressive stress within an ingot during processing is linked directly to the expansions and contractions that accompany the moving zone of two-phase $\gamma + \alpha$ material re-

lated to the phase transformation temperatures (Ar_3, Ar_1, Ac_3, and Ac_1). Thus, incorporating the effect of this phase transformation, including kinetics, into the stress model is very important.

2. The most dramatic changes in stress development occur during the early stages of reheating in the soaking pit.

3. Including the effects of time-dependent plastic flow into the model through a temperature and stress dependent plastic-creep function has a profound influence on both the magnitude and qualitative development of stress. Plastic-creep relaxation lowers stress levels in the ingot by an order of magnitude.

4. The plastic-creep strain throughout the ingot is always very low and rarely exceeds 5 pct. This result indicates that crack formation is not due to stress generation alone. Mechanisms for the generation of elevated-temperature ingot cracking problems, such as panel cracks, must involve a significant metallurgical problem such as loss in hot ductility or localized strain concentration in addition to the presence of tensile stresses.

5. While mold corrugations do not have a significant influence on temperature development, they do have an important effect on local stress variations. The maximum tensile stress in the vicinity of the corrugations is generally centered beneath the corrugation ridges, locally increasing the propensity for crack formation.

This mathematical model for calculating the temperature and stress development in solidifying, cooling, and reheating static-cast steel ingots will be applied in future research directed at understanding the complex mechanisms for elevated-temperature defects, such as panel crack formation, that involve both stress generation and metallurgical problems.

NOMENCLATURE

A	area of element (m^2)
Ar_3, Ac_1	austenite to ferrite/pearlite transformation start temperatures for cooling, heating (°C)
Ar_1, Ac_3	austenite to ferrite/pearlite transformation finish temperatures for cooling, heating (°C)
$[B]^e$	element strain-displacement matrix
b	superscript pertaining to external element boundary
$\{d\}$	nodal displacement vector
$[E]$	3×3 elasticity matrix for plane stress
E	elastic modulus (MPa) or (GPa)
e	superscript pertaining to element
$\{F_{\varepsilon_T}\}$	thermal force vector
$\{F_{\varepsilon_p}\}$	plastic strain force vector
$[K_\sigma]$	global stiffness matrix
$[K_\sigma]^e$	element stiffness matrix
L	length (m)
NE	number of elements in mesh
q	heat flux (W m^{-2})
T	temperature (°C)
T_0	base temperature in Eq. [10]
TLE	thermal linear expansion (m m^{-1})
t	time (s)
Δt	time step increment (s)
u, v	incremental displacements in x and y directional (m)

x, y	coordinate directions (m)
α	thermal linear expansion coefficient (m m^{-1} °C^{-1})
α	ferrite/pearlite phase of steel
γ_{xy}	shear strain
γ	austenite phase of steel
$\dot{\varepsilon}_p$	scalar plastic-creep strain rate (m m^{-1} s^{-1})
$\overline{\varepsilon}_p$	positively accumulated total effective plastic strain (m m^{-1})
σ_I, σ_{II}	total principal stresses (MPa)
$\overline{\sigma}$	total effective stress (MPa)
τ_{xy}	shear stress (MPa)
ν	Poisson's ratio
$\{\Delta\varepsilon\}$	incremental total strain vector containing 3 components ε_x, ε_y, γ_{xy} (m m^{-1})
$\{\varepsilon\}$	3×1 total strain vector (m m^{-1})
$\{\Delta\varepsilon_e\}$	incremental elastic strain vector containing 3 components $\Delta\varepsilon_{xe}$, $\Delta\varepsilon_{ye}$, γ_{xye} (m m^{-1})
$\{\Delta\varepsilon_p\}$	incremental plastic-creep strain vector containing 3 components $\Delta\varepsilon_{xp}$, $\Delta\varepsilon_{yp}$, γ_{xyp} (m m^{-1})
$\{\varepsilon_p\}$	3×1 total plastic-creep strain vector (m m^{-1})
$\{\Delta\varepsilon_T\}$	3×1 incremental thermal strain vector (m m^{-1})
$\{\Delta\sigma\}$	incremental stress vector containing 3 components $\Delta\sigma_x$, $\Delta\sigma_y$, $\Delta\tau_{xy}$ (MPa)
$\{\sigma\}$	3×1 total stress vector (MPa)

REFERENCES

1. J. Mathew and H. Brody: *Nuclear Metallurgy*, 1976, vol. 20, Part 2, pp. 978-90.
2. F. G. Rammerstorfer, C. Jaquemar, D. Fischer, and H. Wiesinger: *Numerical Methods in Thermal Problems*, July 1979, pp. 712-22.
3. A. Grill and K. Schwerdtfeger: *Ironmaking and Steelmaking*, 1979, vol. 3, pp. 131-35.
4. A. Palmaers, A. Etienne, and J. Mignon: *Stahl und Eisen*, Sept. 1979, vol. 99, No. 19, pp. 1039-50.
5. J. R. Williams, R. W. Lewis, and K. Morgan: *Int. J. Numer. Methods in Eng.*, 1979, vol. 14, No. 1, pp. 1-9.
6. J. O. Kristiansson: *Journal of Thermal Stresses*, 1982, vol. 5, pp. 315-30.
7. T. Hara: *Tetsu-to-Hagané Overseas*, 1964, vol. 4, No. 3, pp. 296-303.
8. R. H. Tien and V. Koump: *J. Applied Mechanics* (Trans. ASME), 1969, vol. 36, pp. 763-67.
9. K. Sakiu: *Tetsu-to-Hagané*, 1979, vol. 60, No. 12, pp. 1591-98.
10. B. G. Thomas, I. V. Samarasekera, and J. K. Brimacombe: *Metall. Trans. B*, 1987, vol. 18B, pp. 119-30.
11. B. Barber and A. Perkins: *First International Conference on Numerical Methods in Thermal Problems*, Swansea, England, 1979, pp. 691-701.
12. B. G. Thomas, I. V. Samarasekera, and J. K. Brimacombe: *ISS Transactions*, 1986, vol. 7, pp. 21-29.
13. A. Grill and K. Sorimachi: *Int. J. Numer. Methods in Eng.*, 1979, vol. 14, pp. 499-505.
14. O. C. Zienkiewicz and I. C. Cormeau: *Int. J. Numer. Methods in Eng.*, 1974, vol. 8, pp. 821-45.
15. A. Mendelson: *Plasticity—Theory and Applications*, R. E. Krieger Publishing, Malabar, FL, 1968 (reprinted 1983), pp. 213-15.
16. O. C. Zienkiewicz: *The Finite Element Method*, 3rd ed., McGraw-Hill, London, 1977.
17. Y. Yamada, N. Yoshimura, and T. Sakurai: *Int. J. Mech. Sci.*, Pergamon Press, 1968, vol. 10, pp. 343-54.

18. O. C. Zienkiewicz, S. Valliappan, and I. P. King: *Int. J. Numer. Methods in Eng.*, 1969, vol. 1, pp. 75-100.
19. B. G. Thomas: Ph.D. Thesis, University of British Columbia, Vancouver, BC, Canada, 1985.
20. P. J. Wray: *Modeling of Casting and Welding Processes*, AIME Conference Proceedings, 1980, pp. 245-57.
21. G. Forsythe and C. Moler: *Computer Solution of Linear Algebraic Systems*, Prentice Hall, Englewood Cliffs, NJ, 1967.
22. S. R. Bodner and Y. Partom: *J. Applied Mechanics*, 1975, vol. 42, pp. 385-89.
23. E. W. Hart: *J. of Eng. Materials and Technology* (Trans. ASME), 1976, vol. 98, pp. 193-201.
24. L. Anand: *J. of Eng. Materials and Technology* (Trans. ASME), 1982, vol. 104, pp. 12-17.
25. A. Palmaers: *CRM*, Oct. 1977.
26. T. Sakiu and M. Ohashi: *Tetsu-to-Hagané*, 1981, vol. 67, No. 11, pp. 134-43.
27. P. Feltham: *Proc. Roy. Soc.*, 1953, vol. 66, No. 10-B, pp. 865-83.
28. P. J. Wray: E. C. Bain Laboratory for Fundamental Research, US Steel, Monroeville, PA, 1965, No. 1072, and 1968, No. 1113.
29. S. Sakui and T. Sakai: *ISIJ Trans.*, 1977, vol. 63, No. 2, pp. 285-93.
30. B. Y. Pines and A. F. Sirenko: *Soviet Physics — Solid State*, January 1963, vol. 4, No. 7, pp. 1393-99.
31. O. D. Sherby: *Acta Metall.*, 1962, vol. 10, pp. 135-47.
32. J. Robbins, O. C. Shepard, and O. D. Sherby: *JISI*, October 1961, vol. 199, pp. 175-80.
33. G. W. Greenwood and R. F. Johnson: *Proceedings of the Royal Society*, 1965, vol. A283, pp. 403-22.
34. D. M. Keane, C. M. Sellars, and W. J. Tegart: Univ. of Sheffield Dept. of Metallurgy, July 1966.
35. P. J. Wray: *Metall. Trans. A*, 1984, vol. 15A, pp. 2041-58.
36. E. B. Hawbolt, B. Chau, and J. K. Brimacombe: *Metall. Trans. A*, 1983, vol. 14A, pp. 1803-15.
37. O. M. Puhringer: *Stahl und Eisen*, 1976, vol. 96, No. 6, pp. 279-84.
38. W. Köster: *Z. Metalkde.*, 1948, vol. 39, pp. 1-9.
39. C. Boulanger and C. Crussard: *Revue de Metallurgie*, 1956, No. 9, pp. 715-28.
40. D. R. Hub: *Proc. IVth Intern. Cong. Acoustics*, Copenhagen, 1962, No. 551.
41. P. J. Wray: E. C. Bain Laboratory for Fundamental Research, US Steel, Monroeville, PA, June 1965, No. 1054.
42. B. A. Boley and J. Weiner: *Theory of Thermal Stresses*, John Wiley and Sons, Inc., New York, NY, 1960, pp. 272-81, 311.
43. E. P. Popov: *Introduction to Mechanics of Solids*, Prentice-Hall Inc., Englewood Cliffs, NJ, 1968, pp. 316-26.